Characterization of 100Cr6 lattice structures produced by robocasting

M Yetna N'Jock, E Camposilvan, L Gremillard, E Maire, D Fabrègue, D Chicot, K Tabalaiev, J Adrien

Characterization of 100Cr6 lattice structures produced by robocasting

M. Yetna N'Jock [a,*], E. Camposilvan [a,b], L. Gremillard [a], E. Maire [a], D. Fabrègue [a], D. Chicot [c], K. Tabalaiev [a], J. Adrien [a]

[a] Univ Lyon, INSA, MATEIS, METAL, UMR 5510, F-69621 Villeurbanne, France
[b] Department of Materials Science and Metallurgical Engineering, Universitat Politècnica de Catalunya, Av. Diagonal 647, Barcelona, Spain
[c] Université Lille Nord de France, Lille1, LML, UMR 8107, F-59650 Villeneuve d'Ascq, France

HIGHLIGHTS

- Lattice structures of 100Cr6 steel are fabricated from metal-based ink by robocasting using Pluronic F-127 solution
- The proposed ink formulation promoted sintering of printed parts
- The optimization of the heat treatment allowed to reduce the porosity in the printed parts
- Interesting mechanical properties are obtained both at a local level and at the architecture level
- Dense parts are obtained with a regular macroporosity which do not require a complex formulation as reported in literature

GRAPHICAL ABSTRACT

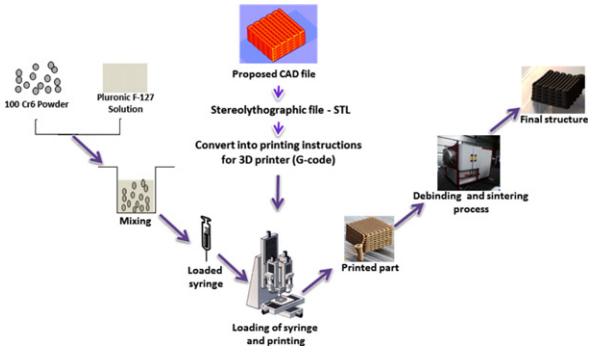

ARTICLE INFO

Article history:
Received 6 December 2016
Received in revised form 2 February 2017
Accepted 20 February 2017
Available online 24 February 2017

Keywords:
Additive manufacturing
Robocasting
Mercury intrusion porosimetry
X-ray micro-tomography
Microstructural characterization
Mechanical properties

ABSTRACT

Lattice structures of 100Cr6 steel were manufactured from metallic-based inks by robotic-assisted deposition (robocasting) using Pluronic F-127 solution. The stability and pseudo-plastic behavior of the ink were optimized, and allowed printing through 200–840 μm nozzles, leading to macroporous architectures composed of 300–600 μm diameter rods separated by 90–350 μm pores, after debinding and sintering. A second level of porosity (sub-micron size) was controlled by adjusting the sintering temperature. The linear shrinkage due to drying and thermal consolidation was evaluated from images obtained by micro-tomography and volumes measured by mercury intrusion porosimetry. Whatever the thermal treatments, the microstructure was always mainly composed of ferrite – α. The mechanical properties were estimated both at a local level (Young modulus and hardness of the rods by nanoindentation, coherent with those of 100Cr6 steel) and at the architecture level (stress-strain curve of the structures, showing a plastic behavior related to a good consolidation of the structure). Thus, dense metallic lattice structures with a regular macroporosity and interesting mechanical properties can be easily obtained with these water-based metallic inks, which do not require a complex formulation nor high organic content as reported in literature.

1. Introduction

Additive Manufacturing (AM) is a set of manufacturing technologies which consists in converting a three-dimensional numerical

* Corresponding author.
E-mail address: michel.yetna_n_jock@utt.fr (M. Yetna N'Jock).

http://dx.doi.org/10.1016/j.matdes.2017.02.066

object obtained by computer-aided design (CAD) or with the help of a three-dimensional scanning system into a physical object by adding matter only where it is needed. During the last decade, AM has received more attention from large fields of applications such as automotive, aerospace, materials sciences, chemistry, biomedical and consumer electronics because of its capability to design and fabricate complex shapes that are difficult or even impossible to obtain using traditional manufacturing approaches [1]. Nowadays, several AM techniques can shape objects made of such materials as photo-polymeric resins, ceramics, paper, wood, composite, biomaterials, with feedstocks available in the form of liquid, paste, sheets … and powders. Starting from powder feedstocks, the most used technologies for AM of metals are powder-bed systems, often referred to as selective laser sintering (SLS) [2], direct metal laser sintering (DMLS) [3], selective laser melting (SLM) [4–5], electron beam melting (EBM) [6] and binder jetting (BJ) [7–9]. These AM systems are capable of producing high-quality, functional and load-bearing parts from a selected range of metallic powders. However, the consolidation methods based on the use of heating source (laser, beam) sometimes lead to poor surface finish [5], high amount of residual stresses, undesirable microstructure and local warping [10]. In addition, these AM technologies offer low control of porosity and are not suitable for the fabrication of spanning lattice structures with fine design.

To overcome the weaknesses of powder-bed AM systems, some authors [11–15] have proposed to use Direct Ink Writing (DIW) techniques such as Robocasting which consists in the continuous extrusion of an ink in the form of filament through a fine nozzle, deposited layer upon layer to fabricate three-dimensional parts. Unlike powder-bed systems, the shaping process relies on the sole rheological properties of inks, which must quickly set after extrusion. Consolidation is then carried out normally by evacuation of the solvent (drying), debinding of additives and sintering of the preform in a furnace. Furthermore, the use of feedstock in form of ink offers the ability to print a wide range of materials at low cost. The architecture and the composition of the robocasted objects are directly linked to the properties and formulations of inks. The latter requires a high solids loading to counteract shrinkage and cracking, homogeneous particle distribution to ensure a constant flow through the nozzle, avoiding flaws due to agglomerates, suitable rheology to ensure shape retention and good welding of the filaments, a binder phase that is easy to burn out and suitable solidification kinetics. Some approaches [16–17] have been explored to meet these criteria. For example, Cesarano [18] formulated concentrated slurries with a maximum solid loading of 60 vol% to minimize drying-induced shrinkage and cracking. In a non-aqueous system, Shao et al. [19] have included many additives in concentrated suspension with a solid loading of 70 vol% to improve sintering and forming behaviors of Nb-TiAl. Schlordtil et al. [20] proposed an aqueous alumina-loaded gel coagulated with ammonium-acetate (NH_4Ac) in order to obtain adequate rheological properties for fabrication of alumina lattice structures. Recently, Jakus et al. [21] developed inks synthetized by creating a mixture of 2-butoxyethanol (2-Bu) and dibutyl phthalate (DBP) (2:1by mass) with added DCM, in which metal or oxide metal powders were dispersed by shaking. This latter suspension was then combined with a solution of PLGA (as binder) dissolved in DCM initially present in excess to promote homogenous mixing of the components. The final inks were 3D-printed into lattice structures using tips of diameter in the 200–840 μm range. Upon sintering in a reducing hydrogen atmosphere, the 3D-printed preforms were consolidated into a metallic objects, avoiding warping or cracking. However, the use of toxic additives may represent a limitation for the use of this formulation, while the presence of large organic contents may limit the densification of parts resulting in a decrease of mechanical properties.

Recently, simpler and non-toxic formulations have been proposed, made by mixing dry powders with a hydrogel composed of water and a poloxamer copolymer [22–24]. In these formulations, the triblock copolymer, composed of polyethylene oxide (PEO) and polypropylene oxide (PPO) in a A-B-A sequence, acts both as a reversible gel former and as a dispersant. Once dissolved in water by 20–30 wt%, the solution exhibits low viscosity between 0 °C and 15 °C and turns into a stiff deformable and reversible gel between 15 °C and 20 °C thanks to the formation of a micelle network. The presence of the network, together with the non-ionic surfactant character of the copolymer, allows the dispersion and stable suspension of high volume fractions of powder with no need for precise pH control.

In this paper, a flexible ink design comprising a poloxamer-based hydrogel and metallic (100Cr6) powder is used to create 100Cr6 steel lattice structures by mean of Robocasting. The effect of powder content and heat treatment on dimensions, rods size, and densification of steel lattices has been investigated. The microstructure and mechanical properties of sintered steel lattice structures have been characterized in order to determine their potential applications.

2. Experimental section

2.1. Samples preparation

A PEO – PPO poloxamer triblock copolymer (Pluronic - F127, Sigma Aldrich, France) in form of dry granules was initially dissolved in distilled water (30 wt%) to form the hydrogel. The dissolution was done progressively using a magnetic stirrer in a number of mixing steps (10 min each), including a cooling step between each one once the concentration was sufficient to form a gel at room temperature. The gel was finally stored at 3 °C for 6 h, to homogenize it and evacuate all the air bubbles. Subsequently, a dual asymmetric planetary centrifugal mixer (SpeedMixer DAC 150.1 FWZ-K, Flacktek, Germany) has been used to disperse 42 vol% of 100Cr6 steel powder (Sandvik Materials Technology, UK) in the solution. Paste homogeneity was achieved progressively through cycles of cooling at 0 °C and mixing for time intervals between 1 and 10 min. After deairing, the final ink was cooled again in order to become liquid and poured into 5 mL syringes (Nordson EFD, France), avoiding introducing air during the process. Syringes were then stored at room temperature (25 °C). A displacement-controlled plunger (Aerotech, USA) was used to extrude the paste in form of filament through conical polypropylene nozzles of several diameters (840 μm, 540 μm, 410 μm) connected to the syringe tip.

The ink was deposited on a flat glass substrate (4 mm of thickness) previously coated with hydrophobic Teflon-based grease, using a Cartesian gantry system (Aerotech, USA) adapted for DIW. The humidity in the printing environment was maintained higher than 80% to avoid tip clogging and unwanted deformation of the piece during printing. After printing, the samples were first dried at room temperature during 24 h and easily removed from glass substrate. Thermo-gravimetric analysis of the hydrogel was performed at heating rate of 2 °C min^{-1} under air atmosphere and thermal debinding of the printed 100Cr6 lattices was carried out in air (heating rate: 2 °C min^{-1}; plateau at 500 °C for 60 min, cooling rate: 5 °C min^{-1}). Finally, sintering was carried out at both 950 °C and 1070 °C in a vacuum furnace to obtain the final structure (heating rate 2 °C min^{-1}; cooling rate 100 °C h^{-1}). In this paper, the 100Cr6 steel lattice structures are referenced to as SL950 and SL1070 for samples sintered respectively at 950 °C and 1070 °C.

2.2. Rheological tests

Rheological tests were performed on a Kinexus Pro + rotationial rheometer (Malvern Instruments Ltd., England) with a plate-on-plate configuration and a gap of 0.5 mm, using an upper plate diameter of

40 mm and roughened surfaces to minimize the possibility of slip. The viscosity was recorded as a function of the shear rate at regular points during a flow ramp from 0.1 s^{-1} to 100 s^{-1}, allowing a stabilization time of minimum 10 s before taking each measurement. The viscoelastic properties of the inks were characterized by stress-controlled oscillatory tests at a frequency of 2 Hz, varying the stress from 1 to 2000 Pa and recording the storage (G′) and loss (G″) modulus, respectively the elastic and viscous components of the complex shear modulus.

2.3. X-ray micro-tomography and mercury intrusion porosimetry

The micro-tomographic measurements have been performed by using a polychromatic X-Ray beam at an accelerating voltage of 155 kV including a current beam of 110 μA and a voxel resolution of 10 μm. The specimen was conducted with 360° rotation around its vertical axis in order to provide the set of projections necessary for tomography reconstruction. A total of 900 projections were recorded with exposure time of 667 ms. After reconstruction the volume was saved as raw file and forward saved as a stack of image converted to grayscale (compression 8-bit TIFF files).The stacks of slices were processed to obtain 3D images using ImageJ. This procedure for image processing of the acquired stacks of image includes cropping a region of interest, filtering, thresholding, binarization and extraction of microstructure characteristics from 3D image. The region of interest to reconstruct in 3D image was selected by removing the entire area around the object in the preview window. Concerning the filtering operation, median filter has been used allowing to eliminate noise to improve the grayscale contrast between voxels representing solid phase (rods) and those representing gaseous phase (macro pores). Manual thresholding was made from histogram to convert grayscale images to binary images. These later are converted into a VTK file using the ImageJ plugin 3D IO for 3D reconstruction with ParaView software. Qualitative and quantitative image analysis were employed to measure rods size distribution, the space between filaments (macroporosity) and damage present in parts, by using the software ParaView (http://www.paraview.org/) and Fiji (http://fiji.sc/Fiji). The lattice rods size distribution and macroporosity were measured using the ImageJ plugins local thickness and stack total fraction from the 3D reconstructed image.

Due to the low voxel size resulting from tomography measurements, mercury intrusion porosimetry has been performed to characterize accurately the microporosity (voids inside the filaments) of SL950 and SL1070. The measurements were made using a high-pressure mercury porosimeter (Autopore IV, Verneuil en Halatte - France), with controlled pressure of up to 400 MPa corresponding to pore access diameters from 0.003 to 1100 μm. The technique is based on the intrusion of a non-wetting liquid (mercury) into open pores under controlled pressure. Both the volume of intruded mercury and the pressure to achieve the intrusion are measured. Therefore it is possible to plot cumulative pore volume versus pore-access diameter, thereby producing a pore-size distribution curve. From this curve, the volume of intruded mercury is used to determine porosity at any pressure.

2.4. Microstructural characterization

The microstructure of SL950 and SL1070 samples was investigated by means of Scanning Electron Microscopy (SEM) (Leo Supra 35 field emission gun, Zeiss, Jena – Germany, with) at 15 kV voltage on polished surfaces. To avoid bending or breaking of walls during the polishing procedure, the space between filaments was filled with molding resin. Subsequently, the samples were mechanically polished and then etched using 3% Nital solution between 10 and 15 s. Chemical analysis was carried out by means of Energy Dispersive X-ray Spectroscopy (EDS) analysis using a Bruker Quantax 70 detector. In order to identify the different phases present in the microstructure of sintered samples, complementary measurements by X-ray diffraction were performed with a Panalytical Empyrean X-ray Diffractometer using Cu Kα radiation (1.5419 Å), in the classical Bragg–Brentano setup. The scanning angle of 2θ was between 20 and 90° with a step size of 0.05°.

2.5. Mechanical testing

The mechanical properties of metallic lattice structure depend on various factors such as density, periodicity or properties of the parent material. In this paper, intrinsic mechanical properties of the parent material used to fabricate the SL1070 sample were evaluated from Nano indentation experiments performed on polished sections of lattice rods employing a nanoindenter XP (MTS, now Agilent 5000, Oak Ridge, TN) equipped with a Berkovich tip. At least 15 indentation tests have been conducted randomly on the polished surface of rods by applying the same indentation tests conditions. Considering the main parameters used, the maximum indentation depth reach by the indenter was fixed at 1000 nm and the strain rate was equal to 0.05 s^{-1}. The harmonic displacement was 2 nm and the frequency equals to 45 Hz. The instrument was operated in the continuous stiffness measurement mode (CSM) allowing the determination of the reduced modulus, E_R and the hardness, HIT, of the parent material of SL1070 as a function of the indenter displacement.

The uniaxial compressive test of SL1070 samples printed through 840 μm tip was carried out using testing machine (Instron CMT 4305) at a loading rate of 0.5 mm/min and maximum load of 5KN. The machine is equipped with a load cell that measures the force applied to the test piece and the displacement is determined by measuring the displacement of the crosspiece. The samples were cut in a size of 12 mm × 12 mm × 5.2 mm. Three tests allow the determination of a mean load against displacement curve and compressive yield strength. The compressive yield strength corresponds to the applied force, F, at which a material begins to deform plastically divided by the initial section, S_0. When the displacement is measured directly from the crosspiece, the stiffness of the machine intervenes in the calculation of the strain, which introduces errors in the measurement and makes difficult the calculation of elastic modulus. In this case, it is possible to measure the elastic modulus using X-ray microtomography images scanned throughout uniaxial compression tests. A volume of interest (VOI)

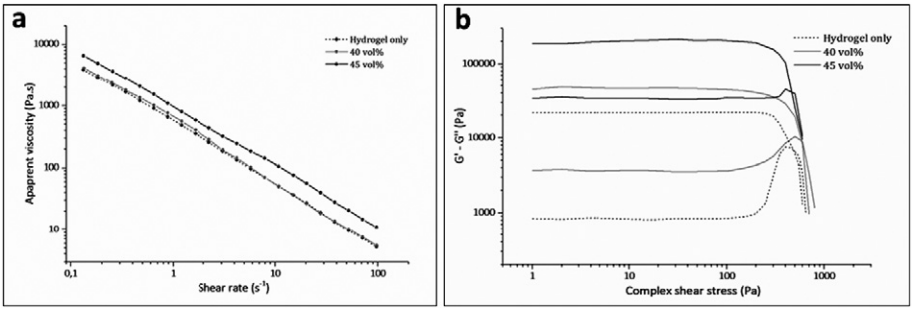

Fig. 1. a) Viscosity/shear rate flow ramp for the sole hydrogel and for the two studied inks. b) Results of the stress-controlled oscillatory tests. For the same group of two lines, G′ and G″ are represented by the line that stands above and below, respectively, in the left area of the chart (viscoelastic region).

consisting of a parallelepiped with a section of 300 voxels × 300 voxels and a height of 300 voxels was cropped in the central portion of the scanned SL1070 images. Digital Image Correlation (DIC) was used as a 3D strain gauge to measure strain using area of interest. Indeed, the Digital Image Correlation (DIC) gives access to the displacement field such that f (x) = g (x + u) on the section of interest and forward the displacement field is then derived to obtain the strain values.

3. Results and discussion

3.1. Rheological behavior of the metallic ink

Viscosity curves appear as straight lines in the double-log plot of the Fig. 1a, showing a clear pseudoplastic behavior. This is a first requirement for printable inks, since it should appear as less viscous when higher shear rate is applied inside the nozzle. The behavior of the sole hydrogel is only slightly different from the Ink at 40 vol%, meaning that at this concentration metallic particles do not produce a significant increase in internal friction, which is only sensed at low shear rates. A curve of the same slope is also observed at 45 vol%, although this time a moderate increase in viscosity is observed for the whole shear rate range. Still, no deviation from the pseudoplastic curve is observed, indicating that probably even higher solid contents could be introduced.

Fig. 1b shows that both the inks and the hydrogel present a significant yield stress comprised between 350 Pa and 500 Pa, which can be identified by the stress at which a sudden decrease in the G′ is observed, or by the point of intersection of G′ and G″. This represents the second requirement for a printable ink to be used in robocasting, since it needs some strength to hold the final shape and not collapse under its own weight. Below the yield point, a viscoelastic region is recognized, where both G′ and G″ have a constant value and G′ is much higher than G″, indicating that in this region the system behaves like a solid body. It is observed that both values increase considerably with the amount of powder dispersed in the ink. Especially if we consider G′, this means that, although the yield stress is similar, inks become stiffer with higher solid content (from ~21 KPa of the sole hydrogel to ~46 KPa for 40 vol% and ~204 KPa for 45 vol%), meaning that they can support open structures with bigger spans.

3.2. Fabrication of 100Cr6 lattice structures

The rheological properties of 100Cr6 steel ink have allowed printing through nozzles diameter in the range of 840–200 μm at reasonable printing speeds. The information concerning the printing parameters of three-dimensional models are listed in Table 1.

Under these conditions, typical steel lattice structures consisting of 10–16 layers in the z-direction, have been obtained. After printing, the samples were first dried at room temperature during 24 h, then debinded and sintered. Thermo-gravimetric analysis of the Pluronic F-127 gel allowed determining the appropriate temperature for the debinding process (Fig. 2).

It is found that the gel begins to lose water at room temperature and the polymer starts to decompose from ~150 °C until ~400 °C. The thermal debinding parameters detailed in the experimental section were chosen accordingly. Finally sintering was carried out at 950 °C and 1070 °C in a vacuum furnace in order to obtain the final metallic lattice structure (heating rate 2 °C min^{-1}; cooling rate 100 °C h^{-1}). Fig. 3(a) shows optical images of SL950 printed with nozzle diameter of 840 μm while Fig. 3(b) represents the 100Cr6 lattice structure after printing with nozzle diameter of 540 μm. In Fig. 3(c), small parts are the 100Cr6 lattice structures printed with nozzle diameter of 200 μm. As shown in Fig. 3(d), the optical observation does not allow measuring accurately contraction through dimensional changes in the length, height and width of the sample before and after sintering. From a general point of view, we can say that no evident change in terms of length can be noticed after sintering. Therefore, this ink formulation allows a good control of the dimensions of the metallic lattice structure as the ink formulation proposed by Run et al. [25]. We also observe that drying and sintering of lattice structures result in the presence of intra-filament pores (1–20 μm) located in the lattice structures rods by SEM observations (Fig. 3e). Apart from these intra-filament pores, it is also found a periodic structure comprised of macropores, which corresponds to the desired architecture (Fig. 3f).

3.3. X-ray microtomographic and mercury intrusion porosimetry analysis

The images of SL950 sample printed with a nozzle diameter of 840 μm were collected from the X-ray microtomography (XRCT) and reconstructed into 2D stacks using Fiji software or 3D images using ParaView 5.0.1 software. Fig. 4 shows the same 2D cross-sectional slice of the inner part after drying (Fig. 4a) and thermal treatment (i.e. debinding and sintering at 950 °C, Fig. 4b). Macropores appear on slices as periodic structures shaped as bands or quadrilaterals, depending on the location of the cross-section inside the body.

It is observed that the slice corresponding to sintered SL950 reveals cracks located in the lattice rods. This may be the result of several factors, such as non-optimized solid loading in the ink and the appearance of residual stresses at some point during drying or heat treatments. For example, as mentioned previously, some authors [18,20] have shown that Robocasting inks require a high solids loading between 60 and 75 vol% to avoid cracking. Indeed, to reduce the risk of cracks, low heating rates are used, resulting in a long debinding time.

Although the thermal debinding process is different for different polymers, a general debinding rate of 0.5 °C min^{-1} or less is sometime proposed to burn out binder [26–27]. Thus, the appearance of cracks in SL950 sample could be justified by the moderate solid loading (42 vol%) and relatively fast debinding rate of 2 °C min^{-1}. Further investigations at different solid loadings and heating rates are needed to explain accurately the origin of these cracks, which are beyond the scope of this work.

Before and after filtering (Fig. 4c), two gray-levels can be easily distinguished: low gray-levels for gaseous phase (macropores) and high gray-levels for solid phase (rods). Therefore, a bimodal histogram characterized by two dominant gray-levels was obtained. To separate gaseous phase from lattice rods a constant threshold of 128 on a scale of 0 to 255 has been chosen. Thresholding of rods using dilation-erosion operations was carried out for filling intra filament pores. Finally binaries images have been obtained with background (black) and foreground (white) which represent macropores and rods respectively (Fig.4d). The thresholded and binarised images are followed by the conversion into a VTK file for 3D reconstruction using ParaView software (Fig. 4e). From subtraction operation between filled filaments and unfilled filaments, it is possible to represent in 2D stacks the intra rods pores (intra filament pores) only and subsequently obtaining their spatial distribution (Fig. 4f).

When measuring the phase volume fraction of the sample shown in Fig. 4d, a constant value of 45% for the solid part of the SL950 rods has been found assuming that closed pores in lattice rods are neglected. Data obtained from the ImageJ plugin “local thickness” allowed obtaining the rods size distribution for SL950 structures printed with

Table 1
Printing parameters of proposed CAD files.

Sample	Nozzle diameter ∅ (mm)	Design dimensions (mm)	Layer height (mm)	Printing speed (mm/s)	Spacing printed line (mm)
lattice structure	0.41–0.84	12 ∗ 12 ∗ (3.1–6.5)	0.75 ∗ ∅	10	1.5 ∗ ∅

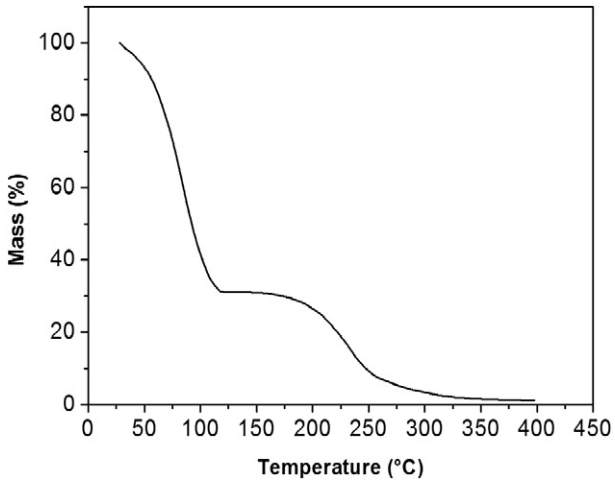

Fig. 2. Thermo-gravimetric analysis of pluronic F-127 gel.

nozzle diameter of 840 μm (Fig. 5a, b and c). Here, the size distribution function of Gauss has been used in the curves fitting of experimental data. The Gaussian distribution known as the normal distribution, has the following function:

$$F(x) = y_0 + \left(\frac{A}{w\sqrt{\pi/2}}\right) e^{(-2((x-x_c)/w)^2)} \quad (1)$$

where y_0 is offset parameter; A is the amplitude and x_c is the arithmetic average of x. The standard deviation of x_c is w/2. The arithmetic average size of lattice rods for SL950 is found to be 725 μm after drying (Fig. 5a) while it is rather 640 μm after sintering (Fig. 5b). Linear shrinkage was calculated according to that difference between the average thickness of lattice rods before and after sintering using the following formula:

$$\text{linear shrinkage} = \frac{R_P - R_S}{R_P} \times 100\% \quad (2)$$

where R_P and R_S are the average thicknesses of lattice rods respectively after printing and sintering. Thus, linear shrinkage certainly due to drying and sintering of SL950 is found to be 13% (Fig. 5c).

Fig. 5d shows the cumulative and the differential intrusion volumes as a function of the pores diameter for SL950 and SL1070 samples. All pores have been assumed as cylindrical and their diameters were calculated by the Washburn equation [28]:

$$D = -4\gamma \cos\varphi / P \quad (3)$$

Assuming a contact angle,φ, of 130° and a surface tension, γ, of 485 dyne cm^{-3}, while pores diameter, D is in μm and the pressure of intruding liquid, P, in Pa. The point A represents the moment where mercury envelops the sample. From A to B, under low pressure, mercury enters the macro pores located between lattices rods, while from B to C, high pressures force mercury to enter micropores, cracks, crevices, or voids of the lattice rods. Point A is sometime used to determine bulk or envelope volume, points A and B are used to determine interparticles void volume (inter-strut volume), and points A and C are used to determine skeletal volume [29]. Therefore, the first intrusion located between A and B corresponds to the entry of mercury into the designed macropores of size in the range of 350–90 μm for both SL950 and SL1070 samples. The second intrusion observed in the SL950 sample represents around 0.15 mL g^{-1} of micropores probably undetectable by XRCT and not detected in sample SL1070. The fact that, a second intrusion is not observed for the sample SL1070 shows that only the designed macropores remains and no additional defect of size in the

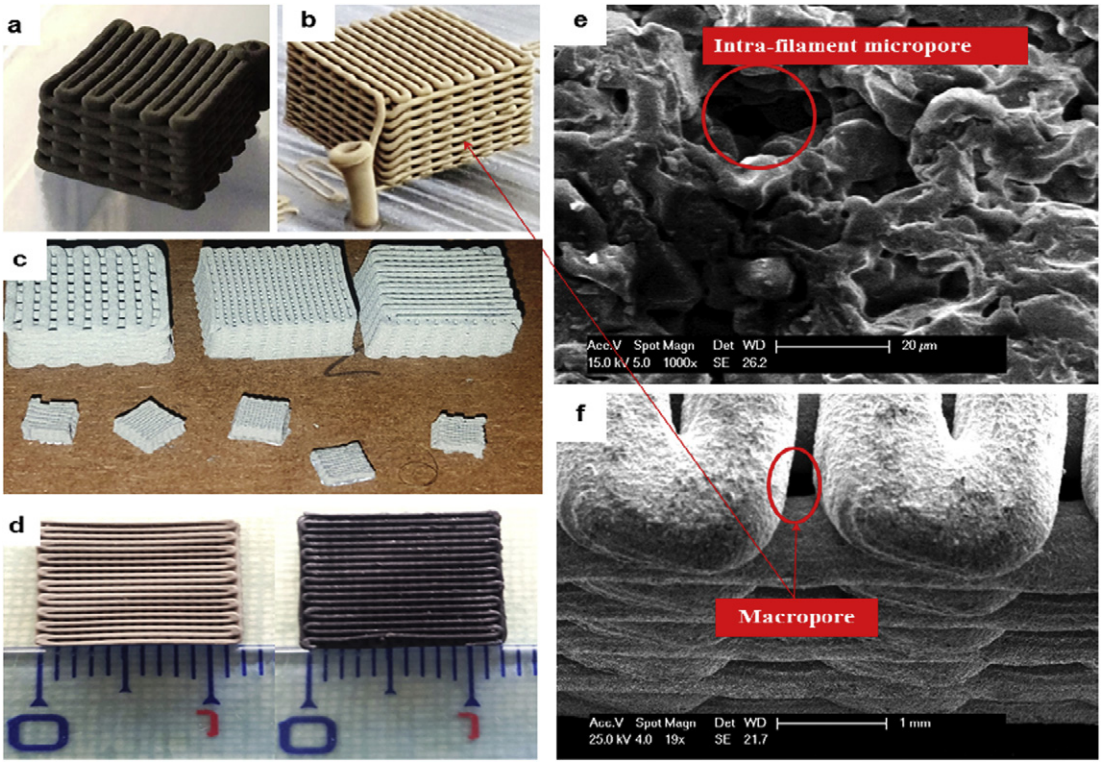

Fig. 3. a) Optical image of debinded and sintered lattice structure printed with nozzle diameter of 840 μm. b) Lattice structure after printing with nozzle diameter of 540 μm. c) Optical image of 100Cr6 lattice structures printed with different nozzle diameters ranging from 840 to 200 μm. d) Dimensions after printing and sintering of lattice structures printed with nozzle diameter of 410 μm. e) SEM images of rod surface showing intra-filament pore of SL950 printed with nozzle diameter of 840 μm. f) SEM images showing plan printing with macropore located between filaments of dried lattice structure printed with nozzle diameter of 840 μm.

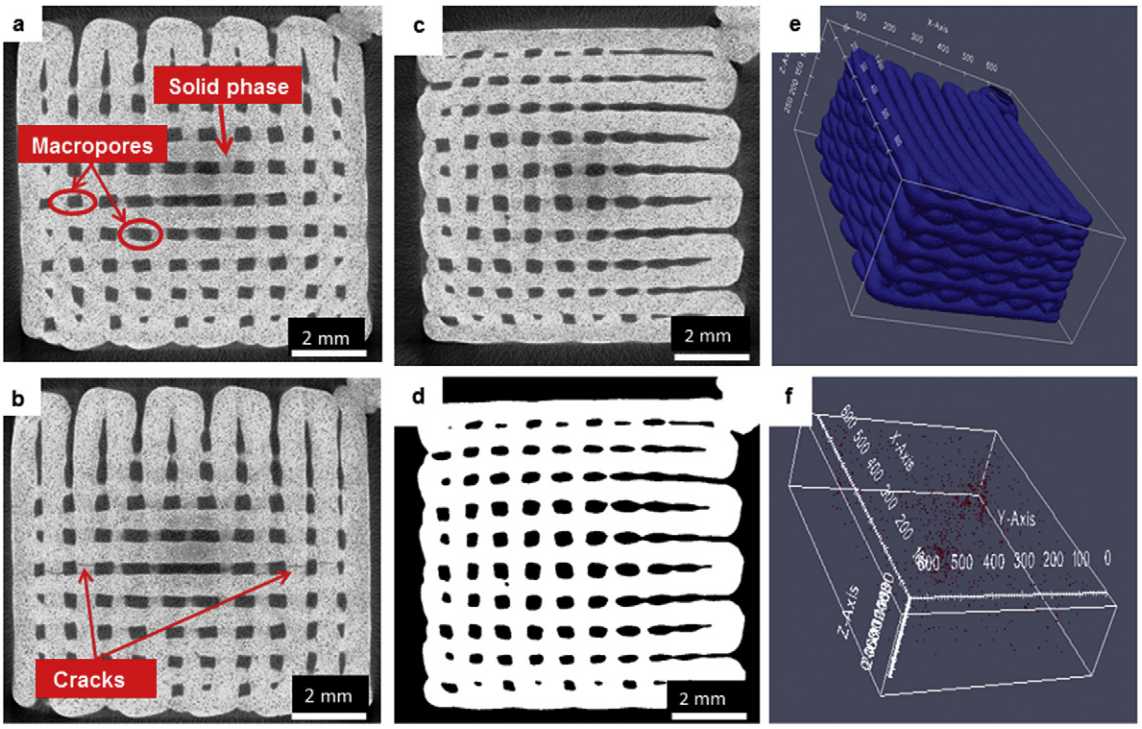

Fig. 4. a) Original micro-tomography images obtained after drying for SL950 printed with nozzle diameter of 840 μm. b) Original micro-tomography images obtained after sintering for SL950 printed with nozzle diameter of 840 μm. c) Micro-tomography images obtained after filtering of the cross-section inside the SL950. d) Thresholded and binarised image of the cross-section inside the SL950. e) Reconstructed 3D image of rods for SL950. f) Reconstructed 3D image of intra-filament pores volume in the solid phase for SL950.

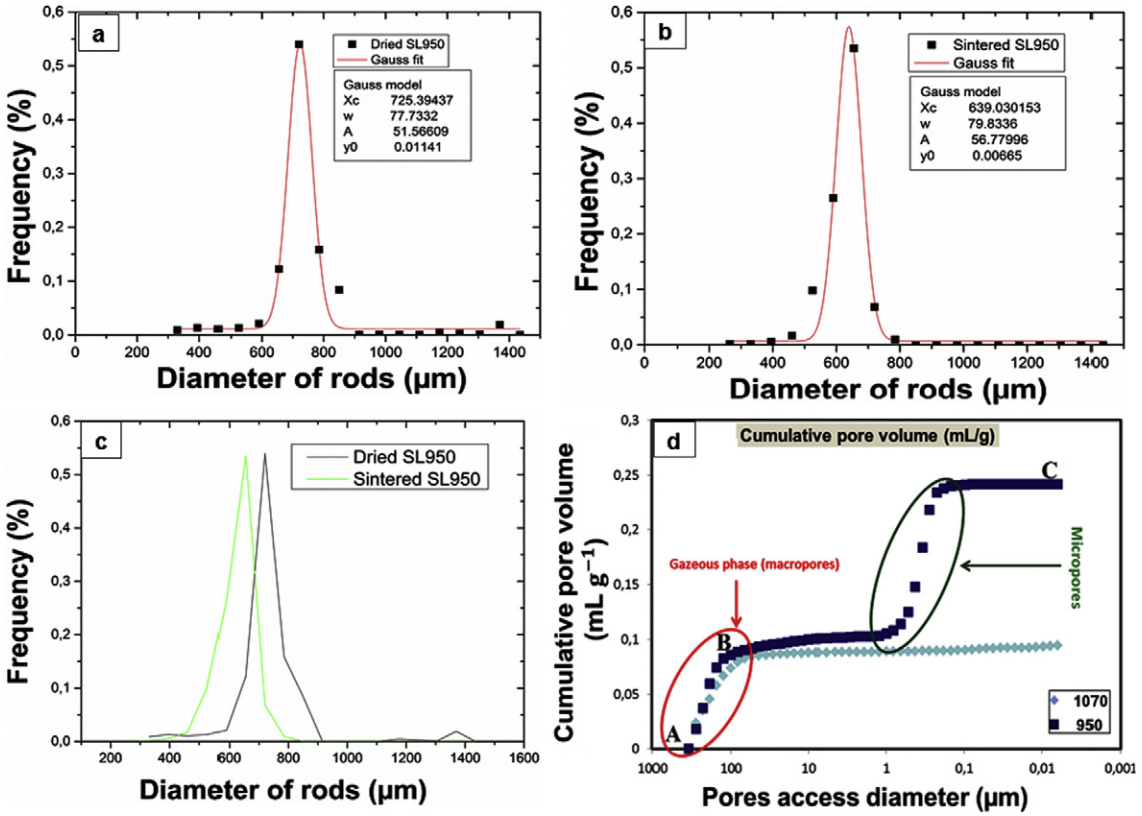

Fig. 5. a) Rods size distribution obtained by microtomography after drying for SL950 structure printed with nozzle diameter of 840 μm. b) Rods size distribution obtained by microtomography after debinding and sintering for SL950 structure printed with nozzle diameter of 840 μm. c) Comparison between rods size distribution of SL950 after drying and sintering. d) Micropores size distribution obtained by mercury intrusion porosimetry for SL950 and SL1070.

range of 80–0.003 μm can be measured in this sample. Assuming that all the micropores are removed during sintering at 1070 °C, only a total intrusion volume of 0.11 mL g^{-1} is found for SL1070 while it is 0.247 mL g^{-1} for SL950. This result corresponds to volume shrinkage of 0.55 ((0.247–0.11)/0.247) i.e. a linear shrinkage of about 0.18, which explains the average thickness differences between SL950 and LS1070. Since porosity is a ratio of pore volume to total volume and density is defined as mass per volume, it is possible to define porosity in terms of density as follow:

$$P_T = (1 - P_B/P_D) \times 100\% \quad (4)$$

P_B is the bulk density and P_D the sample's particle density. SL950 and SL1070 are made of steel then their particles density is assumed to be 7.8 g mL^{-1} according to the literature [30]. To summarize, apparent densities of 0.78 and 3.099 g mL^{-1} were measured for SL950 and SL1070, corresponding to respectively 89% and 60% of porosity.

3.4. Structural characterization

SEM observations using secondary electron mode were performed to analyze the microstructure of SL950 printed with a nozzle diameter of 840 μm (Fig. 6a–b). It is observed that both grains and intergranular zones are darkish in appearance, indicating their similarity in major constituent elements while spherical carbides of bright contrast surrounding these grains are found (Fig. 6a). As observed the microstructure of SL950 reveals high amount of porosities and intergranular zones (Fig. 6a) while for SL1070 larger grains and a significant reduction of the porosity rate and amount of the intergranular zones are found (Fig. 6b). This increase in grains size and decrease of porosity are explained by the faster diffusion occurring at higher temperature (1070 °C).

EDS mapping shows the most important elements (Fe, Cr, C and Si) present in both grains and intergranular zones (Fig. 6c and d) of samples. Fe and Cr distributions are not homogeneous for SL950 (Fig. 6c). There is more Cr in the carbides than in the core of the grains. This suggests that the sintering temperature of 950 °C was not sufficient to achieve the complete diffusion of Cr and Fe. The other components (e.g., Carbon and Silicon) seem homogeneous excepted small regions of porosities observed with very high carbon concentrations. Thus, the sintering at 1070 °C allowed a better diffusion of elements which favors the increase of grains size, more homogeneous distribution of the elements in the sample volume and causes the decrease of the amount of the intergranular zones (Fig. 6d).

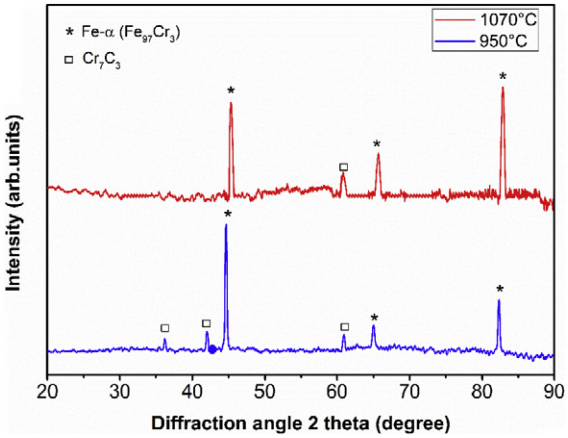

Fig. 7. XRD analysis of SL950 and SL1070 samples.

The identification of phases in specimen was achieved by comparing the specimen diffractograms recorded with those available in powder diffraction file (PDF) in the database ICDD. As observed in Fig. 7, two principal phases were identified for sintered sample: the chromium carbides Cr_7C_3 (PDF# 10897244) and the ferrite-α (PDF# 30654607).

It is observed that high diffraction peaks are attributed to the ferrite-α (PDF# 30654607) mainly composed of iron while weak diffraction peaks are only attributed to the Cr_7C_3 (PDF# 10897244). The decrease in the intensity of all the peaks implies a decrease in the amount of Cr_7C_3. This means that the intergranular zones observed in SEM micrographs would be composed mostly of Cr_7C_3. This result confirms as expected that the sintering at 1070 °C allowed the decrease of the amount of chromium carbides which favors a more homogeneous distribution and a decrease of the number of cracks.

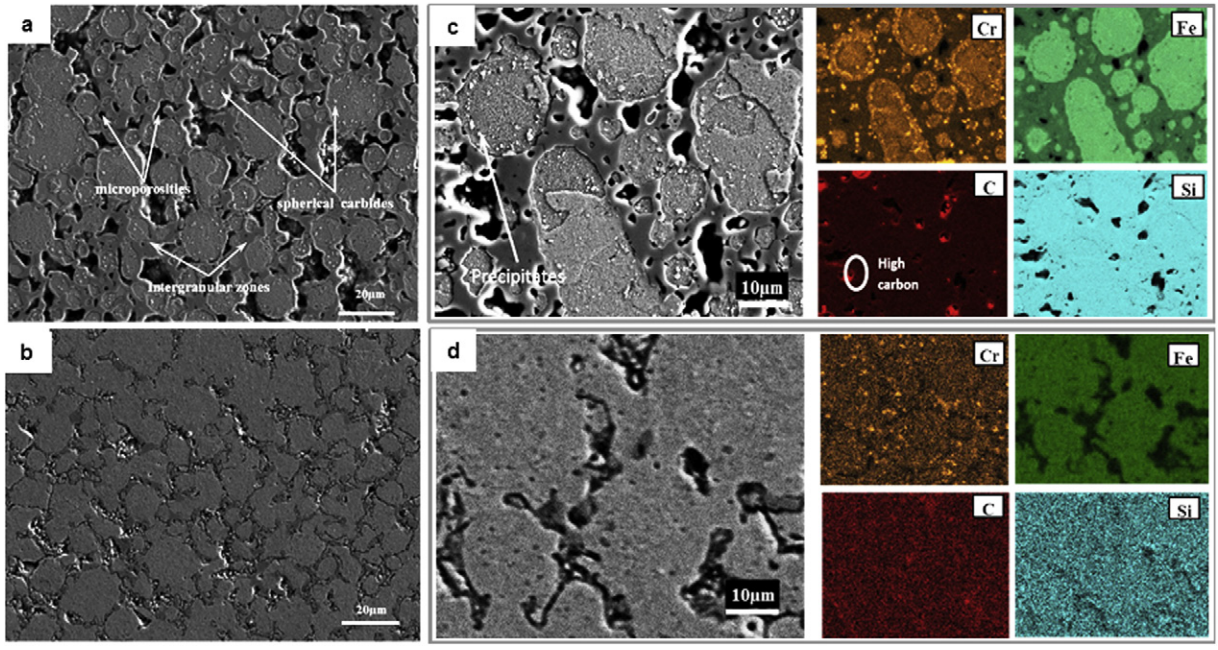

Fig. 6. a) Microstructure observed by SEM of the extruded shape of SL950. b) Microstructure observed by SEM of the extruded shape of SL1070. c) EDS mappings measurements obtained on SL950. d) EDS mappings measurements obtained on SL1070 sample.

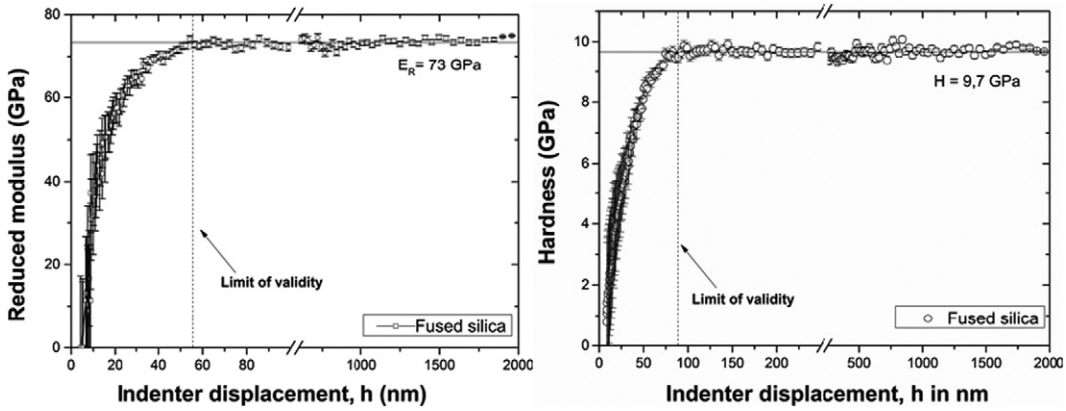

Fig. 8. Reduced modulus and hardness of fused silica as a function of the indenter displacement.

3.5. Mechanical properties of the SL1070 sample

Nanoindentation testing performed in the continuous stiffness measurement mode (CSM) are mostly used to measure the reduced modulus, E_R and the hardness, HIT, of bulk materials or thin films. This mode allows measuring the load applied as a function of indentation depth. In general, the hardness and elastic modulus are obtained from the loading and unloading curves. The hardness, HIT = Pm/A_C, is defined as the ratio between the maximum load, Pm, and a representative contact area between the indenter and the material. The reduced modulus $E_R = (S\sqrt{\pi})/(2\beta\sqrt{A_C})$ is calculated from the slope, *S*, of the unloading part of a load-depth curve [31] with the same contact area, A_C, and a corrective factor, β, which is usually close to 1.05. To take into account the inevitable blunted tip defect, Oliver and Pharr [32] suggested the use of a complex function involving several fitting parameters. Preliminary tests performed on fused silica (calibration sample of the indenter tip defect) show a constant value of 73 GPa for reduced modulus when the indenter penetration reaches a value approximately equal to 55 nm, while the hardness value becomes constant close to 9.7 GPa for indenter penetrations higher than 85 nm (Fig. 8).

These experimental values for the reduced modulus and the hardness are in a good agreement with those obtained in literature for fused silica. It is important to note the in-depth domain of validity for elastic modulus and hardness will be used for the tested sample. The great variation of the mechanical properties before the two limit values of 55 nm and 85 nm for reduced modulus and hardness, respectively, is due to the influence of the blunted indenter tip defect.

In this range of indenter displacements, the complex function due to Oliver and Pharr is not valid. This result has been confirmed by Chicot et al. [33] by plotting the theoretical square root of contact area versus the contact depth. Regarding the number of fitting parameters in the function proposed by Oliver and Pharr [32] and the difficulty to calibrate the contact function area, these authors suggested the use of simplest function involving only the indenter tip defect length. The proposed function gives similar results.

Applied to the tested sample, the reduced modulus and hardness of parent material for SL1070 are represented as a function of the indenter displacement (Fig. 9). It is observed that the reduced modulus is constant and equals to 177 GPa for indenter displacements between 55 to 140 nm with a standard deviation located in the range of ±18% around the mean value. For indenter displacements higher than approximately 140 nm, the reduced modulus regularly decreases. This variation could be attributed to the indentation size effect or damage induced in the material resulting of the process. That is why we only consider the value of 177 GPa for the reduced modulus of the parent material (100Cr6 steel). From the reduced modulus, the elastic modulus of the parent metal, E_{100Cr6}, for SL1070 was determined using the following equation [34]:

$$E_R = 1/\left[(1-\nu^2)/E_{100Cr6} + (1-\nu_i^2)/E_i\right] \quad (5)$$

The respective values of 1141 GPa and 0.07 are taken for the elastic modulus, E_i and Poisson's ratio, ν_i, for Berkovich diamond indenter.

The Poisson's ratio, ν, is taken equal to 0.3 for parent material. The bulk elastic modulus of the parent material has been found equal to ~190 ± 28 GPa. Starting from the contact area proposed by Oliver and Pharr [32], the hardness directly measured on the SL1070 rods can be plotted as a function of the indenter displacement (Fig. 9).

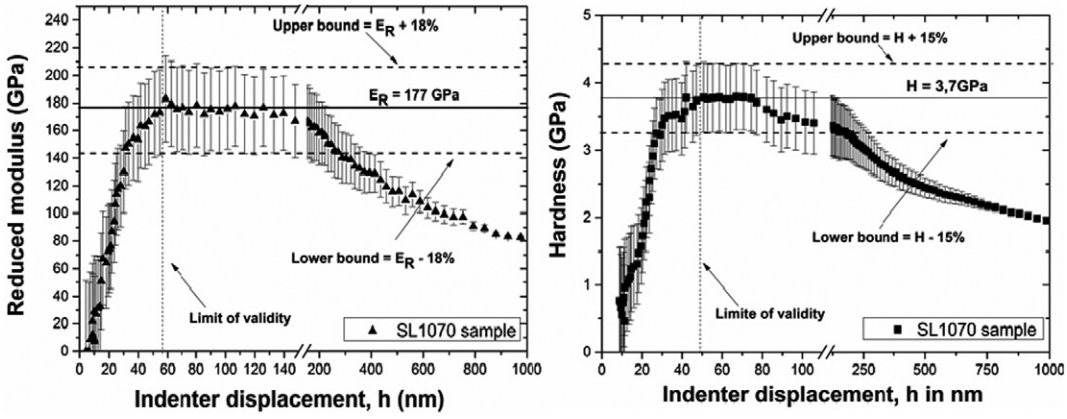

Fig. 9. Reduced modulus and hardness variation of parent material for SL1070 sample.

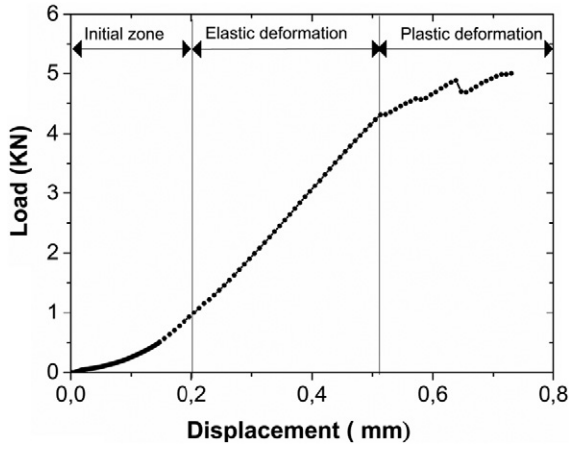

Fig. 10. Force-displacement curve obtained from the average of three compressive tests on SL950 samples.

This figure clearly shows a constant hardness value equals to 3.7 ± 0.6 GPa between 50 and 80 nm. However, this plateau is observed in the domain where the hardness obtained for the calibrated sample is not constant. In practice, it will be more rigorous to analyze hardness variation of indenter displacements higher than approximately 80 nm. However, we clearly see in this figure that the hardness variation tends toward this limit value of 3.7 GPa which can be reasonably considered as the hardness value of the tested sample. On the other hand, we can conclude that hardness seems to be more sensitive to material damage since it varies after indenter displacements higher than 80 nm whereas this value is close to 140 nm for the elastic modulus variation.

Tabor [35] showed that the hardness of several metals is proportional to yield strength with a constant proportionality of approximately 3. Following this approach, the yield strength, σ_{100Cr6}, of the parent material is found to be 1.2 GPa, which is in accordance with the value found in the literature [36]. The elastic modulus, E_{SL1070}, and the yield strength, σ_{SL1070}, of the macroporous lattice structure SL1070 were estimated using the following mechanical models proposed by Gibson and Ashby [37]:

$$E_{SL1070}/E_{100Cr6} = (\rho)^2 \tag{6}$$

$$\sigma_{SL1070}/\sigma_{100Cr6} = 0.3(\rho)^{3/2} \tag{7}$$

where, ρ (= 1-porosity) is the relative density. For the relative porosity of 0.6, the structural modulus and yield stress of SL1070 are estimated to be 30 GPa and 91 MPa.

The compression behavior of the sintered structure was measured during two compression tests. The result of the first test is shown in Fig. 10 for sample SL1070. The strain was crudely measured using the position of the piston, so it cannot be trusted. The only interest of this curve is to show that some plastic deformation can be observed in this sample. The yield strength of the sample is measured to be equal to 30 MPa in compression. This is three times smaller than the value anticipated form the Gibson and Ashby prediction. The discrepancy between the estimated and measured yield strength can be explained by the approximation made on the section and also the Gibson and Ashby assumptions are not checked here (shape of the structure).

A second test was achieved at low strain in situ inside the X-ray tomograph. From the scan of the undeformed and deformed SL1070 images, a measurement of the global deformation of the sample was achieved via digital image correlation (DIC) [38]. The applied load was equal to −3500 N and the surface of the sample perpendicular to the compression direction was equal to 150 mm^2. The applied stress was then equal to 23.2 MPa, so the sample remained in the elastic domain. The strain value obtained for the direction of compression has been found to be −0.000805. This result allowed calculating a structural elastic modulus of 28.8 GPa which is similar to the value estimated using the models proposed by Gibson and Ashby.

4. Conclusion

Metallic lattice structures have been fabricated from metal ink comprised of 100Cr6 powder mixed with a temperature-reversible hydrogel composed of distilled water and a poloxamer polymer Pluronic-127 by Robocasting technologies. The rheological properties of this ink composed of low organic and additives content has facilitated the printing of the lattice structures through nozzles diameter in the range of 840–200 μm. The final metal lattice structures were achieved after debinding and sintering process. It has been found that after heat treatment, parts retained their designed shape. However, the images collected from X-ray microtomography measurements performed on sample sintered at 950 °C revealed the presence of intra-filament pores and cracks in the lattice rods. A simple optimization of sintering at 1070 °C allowed reducing the porosity to 60% with designed pores of size in the range of 350–90 μm whereas the porosity can reach 89% for sintering at 950 °C. The mercury intrusion porosimetry measurements have shown that only the designed porosity remains in optimized parts, observing no additional defect of size in the range of 80–0.003 μm. In these parts, the X-ray diffraction measurements have revealed the presence of significant fractions of the ferrite-α phase, while compression experiments allowed to measure a structural modulus of 28.8 GPa and a yield strength of 30 MPa. These results confirmed the good consolidation of the 100Cr6 lattice structures. Through their architecture and properties, the lattice structures illustrated here could be used as potential H2 reversible storage materials for solid-oxide batteries [21]. Finally, the capacity for this new means to produce 3D architectures with desirable properties, opens possibility for exploring an extensive variety of structural, energy and biomedical applications that would not be technically accessible with existing manufacturing methods.

References

[1] B.G. Compton, J.A. Lewis, 3D-printing of lightweight cellular composites, Adv. Mater. 26 (2014) 5930–5935.
[2] S. Kumar, J. Kruth, Effect of bronze infiltration on laser sintered metallic parts, Mater. Des. 28 (2007) 400–407.
[3] W.E. Frazier, Metal additive manufacturing: a review, J. Mater. Eng. Perform. 23 (2014) 1917–1928.
[4] I. Yadroitsev, A. Gusarov, I. Yadroitsava, I. Smurov, Single track formation in selective laser melting of metal powders, J. Mater. Process. Technol. 210 (2010) 1624–1631.
[5] I. Yadroitsev, Ph. Bertrand, I. Smurov, Parametric analysis of the selective laser melting process, Appl. Surf. Sci. 253 (2007) 8064–8069.
[6] L.E. Murr, Metallurgy of additive manufacturing: examples from electron beam melting, Addit. Manuf. 5 (2015) 40–53.
[7] E. Sachs, M. Cima, P. Williams, D. Brancazio, J. Cornie, Three dimensional printing: rapid tooling and prototypes directly from a CAD model, J. Eng. Ind. 114 (1992) 481–488.
[8] J. Moon, J.E. Grau, V. Knezevic, M.J. Cima, E.M. Sachs, Ink-jet printing of binders for ceramic components, J. Am. Ceram. Soc. 28 (2002) 755–762.
[9] E.M. Sachs, M.J. Cima, P. Williams, D. Brancazio, J. Cornie, Three-dimensional printing: rapid tooling and prototypes directly from a CAD model, J. Eng. Ind. Trans. ASME 114 (1992) 481–4880.
[10] C.B. Williams, J.K. Cochran, D.W. Rosen, Additive manufacturing of metallic cellular materials via three-dimensional printing, Int. J. Adv. Manuf. Technol. 53 (2011) 231–239.
[11] J.E. Smay, G. Gratson, R.F. Shepard, J. Cesarano III, J.A. Lewis, Directed colloidal assembly of 3D periodic structure, Adv. Mater. 14 (2002) 1279–1283.
[12] S. Ghosh, S.T. Parker, X. Wang, D.L. Kaplan, J.A. Lewis, Direct-write assembly of microperiodic silk fibroin scaffolds for tissue engineering applications, Adv. Funct. Mater. 18 (2008) 1883–1889.
[13] M.J. Xu, G.M. Gratson, E.B. Duoss, R.F. Shepherd, J.A. Lewis, Biomimetic silicification of 3D polyamine-rich scaffolds assembled by direct ink writing, Soft Matter 2 (2006) 205–209.
[14] J. Cesarano III, R. Segalman, P. Calvert, Robocasting provides moldless fabrication from slurry deposition, Ceram. Ind. 148 (1998) 94–102.

[15] S.T. Parker, P. Domachuk, J. Amsden, J. Bressner, J.A. Lewis, D.L. Kaplan, F.G. Omenetto, Biocompatible silk printed optical waveguides, Adv. Mater. 21 (2009) 2411–2415.
[16] X. Lu, Y. Lee, S. Yang, Y. Hao, J.R.G. Evans, C.G. Parini, Solvent-based paste extrusion solid free forming, J. Eur. Ceram. Soc. 30 (2010) 1–10.
[17] J.E. Smay, J. Cesarano III, J.A. Lewis, Colloidal inks for directed assembly of 3-D periodic structures, Langmuir 18 (2002) 5429–5437.
[18] J. Cesarano III, Review of robocasting technology, Mater. Res. Soc. Symp. Proc. 54 (1999) 133–139.
[19] H. Shao, X. Liu, Y. Ji, Z. Guo, Near-net shape processing of spherical high Nb-TiAl alloy powder by gelcasting, Int. J. Miner. Metall. Mater. 20 (2013) 1076–1080.
[20] T. Schlordt, S. Schwanke, F. Keppner, T. Fey, N. Travitzky, P. Greil, Robocasting of alumina hollow filament lattice structures, J. Ceram. Sci. Tech. 33 (2013) 3243–3248.
[21] A.E. Jakus, S.L. Taylor, N.R. Geisendorfer, D.C. Dunand, R.N. Shah, Metallic architectures from 3D-printed powder-based liquid inks, Adv. Funct. Mater. 25 (2015) 6985–6995.
[22] J. Franco, P. Hunger, M.E. Launey, A.P. Tomsia, E. Saiz, Direct write assembly of calcium phosphate scaffolds using a water-based hydrogel, Acta Biomater. 6 (2010) 218–228.
[23] Q. Fu, E. Saiz, A.P. Tomsia, Direct ink writing of highly porous and strong glass scaffolds for load-bearing bone defects repair and regeneration, Acta Biomater. 7 (2011) 3547–3554.
[24] E. Feilden, E.G.T. Blanca, F. Giuliani, E. Saiz, L. Vandeperre, Robocasting of structural ceramic parts with hydrogel inks, J. Eur. Ceram. Soc. 36 (2016) 2525–2533.
[25] X. Ren, H. Shao, T. Lin, H. Zheng, 3D gel-printing—an additive manufacturing method for producing complex shape parts, Mater. Des. 101 (2016) 80–87.
[26] C.F. Escobar, Natal - RN, Effects of Thermal Debinding on Binder Removal of Stainless Steel AISI 420L Feedstock, 08, Congresso Latino Americano de Órgãos Artificiais e Biomateriais, 2012.
[27] M.A. Dos Santos, M.P. Neivock, A.M. Maliska, A.N. Klein, J.L.R. Muzart, Plasma debinding and pre-sintering of injected parts, J. Mater. Res. 7 (2004) 505–511.
[28] E.W. Washburn, Note on a method of determining the distribution of pore sizes in a porous material, Proc. Natl. Acad. Sci. 7 (1921) 115–116.
[29] P.A. Webb, An Introduction to the Physical Characterization of Materials by Mercury Intrusion Porosimetry With Emphasis on Reduction and Presentation of Experimental Data, Micromerietics Instrument Corp, Norcross, Georgia, 2001.
[30] G. Elert, Density of steel. Retrieved (2009)
[31] S.I. Bulychev, V.P. Alekhin, M.Kh. Shorshorov, A.P. Ternovskii, G.D. Shnyrev, Determining young's modulus from the indentor penetration diagram, Ind. Lab. 41 (1975) 1409–1412.
[32] W.C. Oliver, G.M. Pharr, An improved technique for determining hardness and elastic modulus using load and displacement sensing indentation experiments, J. Mater. Res. 7 (1992) 1564–1583.
[33] D. Chicot, M. Yetna N'Jock, E.S. Puchi-Cabrera, A. Iost, M.H. Staia, G. Louis, R. Aumaitre, A contact area function for Berkovich nanoindentation: application to hardness determination of a TiHfCN thin film, Thin Solid Films 558 (2014) 259–266.
[34] M. Yetna N'jock, D. Chicot, J.M. Ndjaka, J. Lesage, X. Decoopman, F. Roudet, A. Mejias, A criterion to identify sinking-in and piling-up in indentation of materials, Int. J. Mech. Sci. 90 (2015) 145–150.
[35] D. Tabor, The physical meaning of indentation and scratch hardness, Br. J. Appl. Phys. 7 (5) (1956) 159–166.
[36] 100Cr6 steel plate, 100Cr6 sheet, 100Cr6 coil-Carbon steel, http://www.steelss.com 2017.
[37] L.J. Gibson, M.F. Ashby, Cellular Solids Structure and Properties, Cambridge University Press, Cambridge, UK, 1997 (Online ISBN: 9781139878326).
[38] J. Réthoré, S. Roux, F. Hild, An extended and integrated digital image correlation technique applied to the analysis of fractured samples: the equilibrium gap method as a mechanical filter, Comput. Mech. 18 (3–4) (2009) 285–306.